CONF-900163--4

UCRL-102731
PREPRINT

The Amos Wakefield Code

J. F. DeFord
G. D. Craig
R. R. McLeod

This paper was prepared for presentation at the Workshop on Accelerator Computer Codes, Los Alamos National Laboratory, Los Alamos, New Mexico, January 22-25, 1990.

January 23, 1990

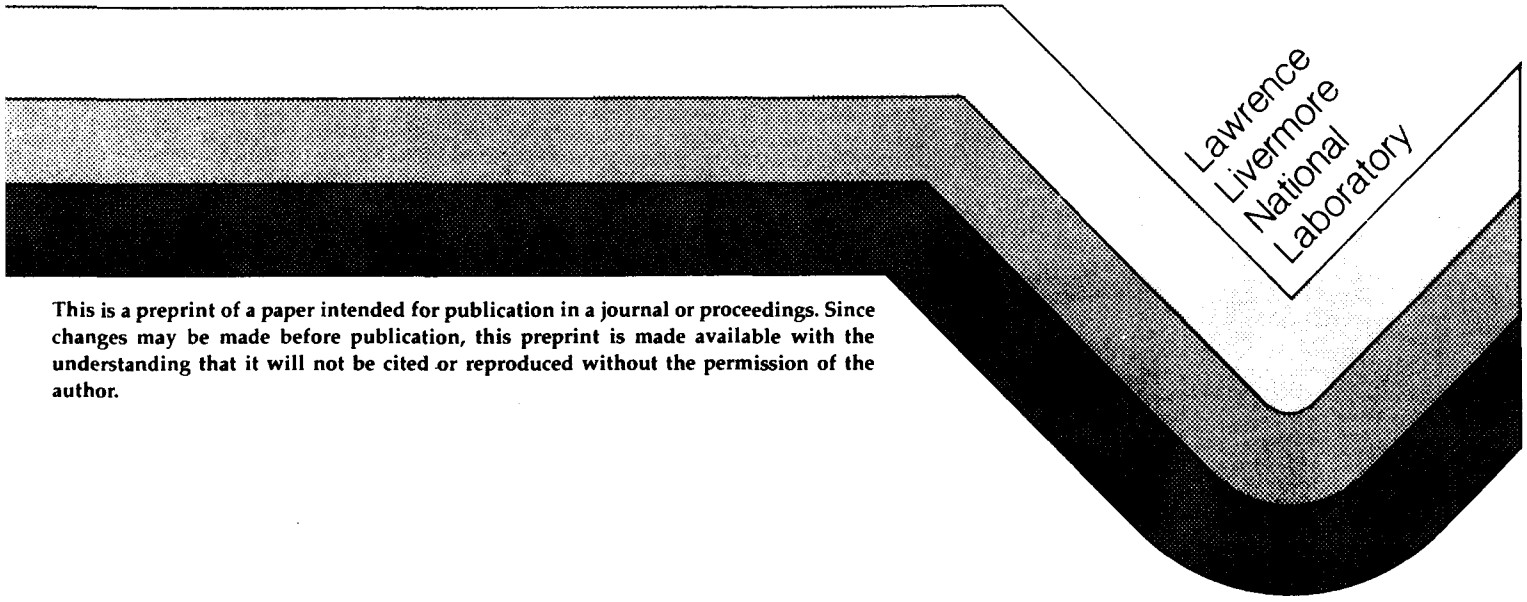

The AMOS Wakefield Code*

UCRL--102731

DE90 007859

J. F. DeFord, G. D. Craig, and R. R. McLeod
LLNL, Livermore, CA 94550

Abstract

AMOS (Azimuthal MOde Simulator) is an electromagnetic simulation computer program that has been developed to study and design accelerator cavities. AMOS simulates the temporal evolution of fields in rotationally symmetric volumes, using a harmonic expansion in the azimuthal coordinate (ϕ) to project the fields onto a two-dimensional, $r - z$, finite-difference grid. An interactive preprocessor has been developed which allows the user to easily construct AMOS grids from geometric models. A wakefield postprocessor has also been developed to compute wake potentials and impedances from AMOS time-domain data. Graphical postprocessing software is presently under development. AMOS has been used to study accelerating modules in several linear accelerators, including the Advanced Test Accelerator (ATA), the Experimental Test Accelerator-II (ETA-II), SNOMAD, Dual Access Radiographic Hydrodynamics Test facility (DARHT), and others. Ongoing AMOS development objectives include the installation of an "open" boundary condition (Lindman), an rf tensor ferrite model, and the extension of AMOS to irregular, boundary conforming grids.

1. Introduction

AMOS (Azimuthal MOde Simulator) [1] is a $2\frac{1}{2}$-D, finite-difference time-domain (FDTD), electromagnetic simulation computer code used primarily in the design of induction linear accelerator (linac) cavities. AMOS simulates the temporal evolution of electromagnetic fields in rotationally symmetric volumes, commonly called "bodies of revolution", by using the FDTD algorithm on fields distributed on a 2-D ($r - z$) grid (Fig. 1). The projection of the fields in the volume onto this 2-D grid is accomplished by expanding the fields in a Fourier series in the third cylindrical coordinate (ϕ) (see Section 2). AMOS solves for the temporal evolution of each mode, or term in the series, independently. For this reason, AMOS is referred to as a "$2\frac{1}{2}$-D" simulation code. AMOS considers the simulation grid to be composed of a set of rectangular subgrids, each having a single set of

* Work performed jointly under the auspices of the U. S. Department of Energy by Lawrence Livermore National Laboratory under contract W-7405-ENG-48, for the Strategic Defense Initiative Organization and the U. S. Army Strategic Defense Command in support of SDIO/SDC-ATC MIPR No. W43-GBL-0-5007.

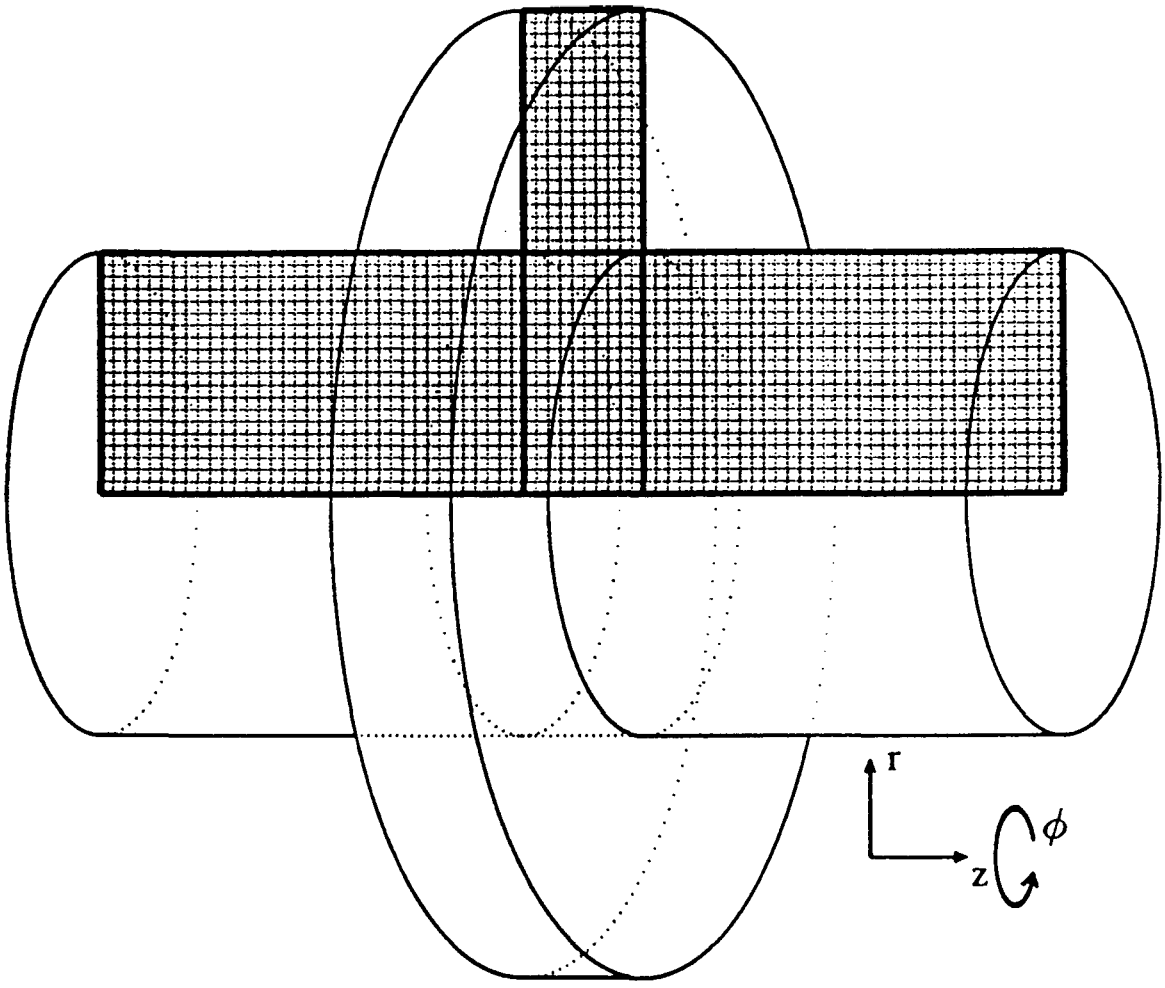

Fig. 1. AMOS simulation volume and corresponding field grid. AMOS models the fields in a cylindrical volume by distributing the field components (E_r, E_ϕ, E_z, H_r, H_ϕ, and H_z) in each rectangular cell in an r - z grid, and assuming the fields have a harmonic ϕ-variation.

electrical properties (ϵ, σ, and μ) which apply to every cell within the subgrid. Radiation or impedance boundary conditions can be applied on the boundaries of the simulation grid as necessary. Both electric and magnetic currents ($\vec{J}$ and $\vec{K}$) may be used as sources for the electromagnetic fields, or the $\vec{E}$ and $\vec{H}$ fields may be driven directly. The user can request output on any field component at any specified time interval at any position within the simulation volume. Desired output positions that do not correspond to a node on the grid or to a particular time step are interpolated from adjacent values.

An interactive, window-based preprocessor (called DRAGON) has been developed to simplify the user definition of the simulation grid. It allows the user to define the problem geometry by entering a series of points, either by moving a cursor around on the graphics screen, or via an input file, or even directly from a CAD system (Fig. 2). The program connects the points with line segments as they are entered. The user may then edit the geometry through a variety of operations such as moving points, moving line segments (collections of points), rotating line segments, adding and deleting points, etc. The final model is composed of a set of closed polygons, each made up of three or more line segments. Once the model geometry is complete, the user specifies the material type in each polygon. The preprocessor then constructs a FDTD grid which closely approximates the model geometry. This grid is subsequently divided into a set of subgrids, and the subgrid definitions are written to a file which becomes part of the AMOS input specification.

A computational postprocessor has also been developed, which allows the user to carry out a variety of operations on the field data generated by AMOS. The purpose of this program is to act as an interface between binary data file dumped by AMOS and a graphical postprocessor still under development. One simple example of the operations performed by the postprocessor is the extraction of a time history of a particular field component from the AMOS output file, which may then be output in standard ASCII to a file for plotting. A time series may also be manipulated before being output. The supported manipulations include Fourier transforms and algebraic operations. The latter

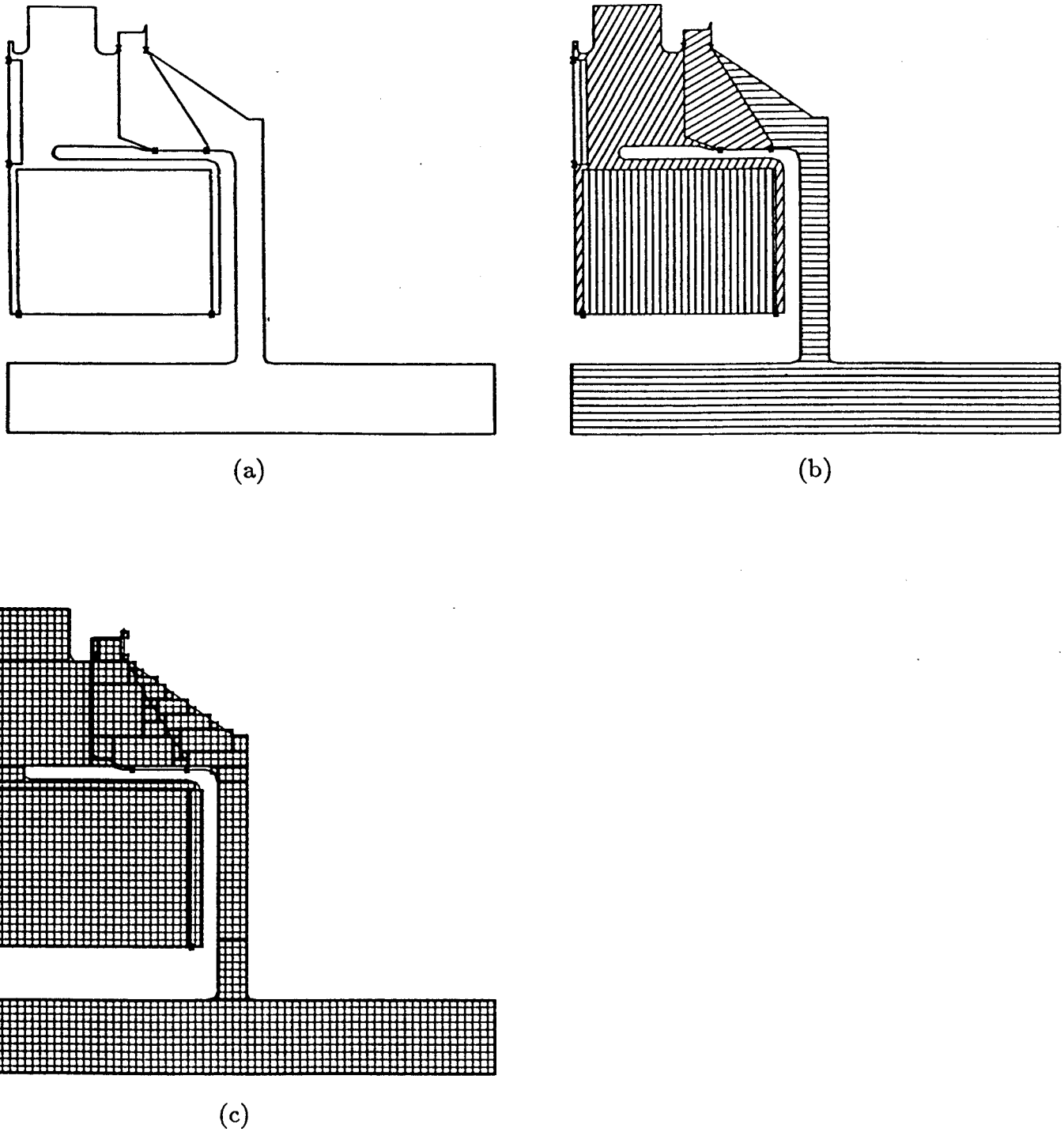

Fig. 2. Model development example using AMOS preprocessor DRAGON. (a) Line segment definition of the model boundaries. The points are entered via mouse, keyboard, or input file. The resulting figure may be edited as necessary. (b) Material specification is made by placing the graphics cursor in each region and entering the material type for that region. (c) Finally, the finite-difference grid is generated to fill the simulation area. The grid is composed of rectangular subgrids, each with a particular material type (ϵ, μ, σ). The specification for this grid is then written into a data file, and this file is included as part of the AMOS input file.

include multiplication by a constant or another series, addition and subtraction of series, etc. More sophisticated operations may be performed involving several time series at once, including the calculation of wake potentials and impedances (see Section 3), two quantities that are important for understanding the interaction of a charged particle beam with a structure such as an accelerator induction cell [2,3,4].

2. Field Equations

The following equations are solved in the time domain by AMOS:

$$\nabla \times \vec{H} = \vec{J} + \dot{\vec{D}} + \vec{J}_s, \tag{1}$$

$$\nabla \times \vec{E} = -\dot{\vec{B}} - \vec{K}_s, \tag{2}$$

$$\nabla \cdot \vec{B} = \rho_m, \tag{3}$$

$$\nabla \cdot \vec{D} = \rho_e, \tag{4}$$

where $\vec{J}_s$ is the impressed electric source current, $\vec{K}_s$ is the impressed magnetic source current, ρ_e is the electric charge density, and ρ_m is the (fictitious) magnetic charge density. All units are MKSA. The linear, scalar, frequency independent constitutive relationships are

$$\vec{B} = \mu \vec{H}, \tag{5}$$

$$\vec{D} = \epsilon \vec{E}, \tag{6}$$

$$\vec{J} = \sigma \vec{E}, \tag{7}$$

where μ is the permeability, ϵ is the permittivity, and σ is the conductivity. The impressed sources are prescribed by the user.

AMOS solves Maxwell's equations in cylindrical coordinates for problems involving rotationally invariant geometries. An explicit azimuthal (ϕ) dependence is assumed to project the fields in the 3-D geometry onto the 2-D, $r - z$ plane. Specifically, the ϕ-dependence of the fields is expanded in harmonic multipoles, and AMOS may be used

to simulate the temporal evolution of the particular multipole of interest. Let the field components all have expansions of the form

$$\vec{f} = \sum_{m=0}^{\infty} \left(\vec{f}_m^{\,p} \cos(m\phi) + \vec{f}_m^{\,q} \sin(m\phi) \right), \tag{8}$$

where $\vec{f}$ represents any of the simulated fields, and the amplitudes $\vec{f}_m^{\,p}$ and $\vec{f}_m^{\,q}$, which are both functions of r, z, and t, are real. To obtain the equations that AMOS solves, we substitute (8) into (1) and (2), which yields four equations that must be satisfied for each multipole number m:

$$\frac{m}{r}\hat{\phi} \times \vec{H}_m^{\,q} + \nabla \times \vec{H}_m^{\,p} = \sigma \vec{E}_m^{\,p} + \epsilon \dot{\vec{E}}_m^{\,p} + \vec{J}_{sm}^{\,p}, \tag{9}$$

$$\frac{-m}{r}\hat{\phi} \times \vec{H}_m^{\,p} + \nabla \times \vec{H}_m^{\,q} = \sigma \vec{E}_m^{\,q} + \epsilon \dot{\vec{E}}_m^{\,q} + \vec{J}_{sm}^{\,q}, \tag{10}$$

$$\frac{m}{r}\hat{\phi} \times \vec{E}_m^{\,q} + \nabla \times \vec{E}_m^{\,p} = -\mu \dot{\vec{H}}_m^{\,p} - \vec{K}_{sm}^{\,p}, \tag{11}$$

$$\frac{-m}{r}\hat{\phi} \times \vec{E}_m^{\,p} + \nabla \times \vec{E}_m^{\,q} = -\mu \dot{\vec{H}}_m^{\,q} - \vec{K}_{sm}^{\,q}. \tag{12}$$

Writing out the individual components of Eqns. (9)-(12) yields twelve equations that must be satisfied. However, *for problems involving linear, scalar constitutive relations*, these twelve equations may be written as two independent sets of six equations each. The solutions of each independent equation set are themselves separate components of a particular azimuthal mode, in the same sense that each azimuthal mode may be decomposed into its TE and TM components. However, these solutions are different from TE and TM modes in that they each contain E_z and H_z, making them hybrid modes. The equations are shown below:

$$\frac{\pm m}{r} H_z^{q,p} - \frac{\partial H_\phi^{p,q}}{\partial z} = \sigma E_r^{p,q} + \epsilon \dot{E}_r^{p,q} + J_{sr}^{p,q}, \tag{13}$$

$$\frac{\partial H_r^{q,p}}{\partial z} - \frac{\partial H_z^{q,p}}{\partial r} = \sigma E_\phi^{q,p} + \epsilon \dot{E}_\phi^{q,p} + J_{s\phi}^{q,p}, \tag{14}$$

$$\frac{1}{r}\frac{\partial}{\partial r}(r H_\phi^{p,q}) \mp \frac{m}{r} H_r^{q,p} = \sigma E_z^{p,q} + \epsilon \dot{E}_z^{p,q} + J_{sz}^{p,q}, \tag{15}$$

$$\frac{\mp m}{r} E_z^{p,q} - \frac{\partial E_\phi^{q,p}}{\partial z} = -\mu \dot{H}_r^{q,p} - K_{sr}^{q,p}, \tag{16}$$

$$\frac{\partial E_r^{p,q}}{\partial z} - \frac{\partial E_z^{p,q}}{\partial r} = -\mu \dot{H}_\phi^{p,q} - K_{s\phi}^{p,q}, \tag{17}$$

$$\frac{1}{r}\frac{\partial}{\partial r}(r E_\phi^{q,p}) \pm \frac{m}{r} E_r^{p,q} = -\mu \dot{H}_z^{q,p} - K_{sz}^{q,p}. \tag{18}$$

The new subscripts on the field quantities indicate which component is represented; r refers to radial component, ϕ refers to azimuthal component, and z refers to axial component. That the fields are actually modal coefficients is implicit in Eqns. (13) - (18), and for the rest of this section. One set of equations is obtained by selecting the upper sign (where two signs are present), and also selecting the first superscript (p or q). The other set is obtained with the lower sign and second superscript. Note that none of the field quantities appear in both sets of equations. By restricting our attention, without loss of generality, to those sources which may be represented purely in one set or the other, we may carry out the simulation using only six equations, with the corresponding reduction in computer time. Note also that if nonlinear constitutive relations were used, then the sets of equations may be coupled through the material model.

The field components are distributed spatially in a computational cell as shown in Fig. 3. Central differencing is used in both space and time to obtain the finite difference equations, and these expressions are integrated explicitly. Because central time differencing is used, the various fields must exist at different time points, just as they must exist at different spatial locations. Specifically,

all components of $\vec{E}$ and $\vec{K}_s \longrightarrow$ integer time steps, i.e., 0, 1, 2,..., k, $k+1$,...,

all components of $\vec{H}$ and $\vec{J}_s \longrightarrow$ half-integer time steps, i.e., $\frac{1}{2}$, $\frac{3}{2}$,..., $k-\frac{1}{2}$, $k+\frac{1}{2}$,....

The given distribution of field components in time and space yields the following set of field updating equations using the standard explicit leapfrog technique [5]:

$$E_{r(i,j)}^{k+1} = \frac{\frac{\pm m}{(j-1/2)\Delta r} H_{z(i,j)}^{k+1/2} - \frac{1}{\Delta z}\left[H_{\phi(i+1,j)}^{k+1/2} - H_{\phi(i,j)}^{k+1/2}\right] - E_{r(i,j)}^{k}\alpha^{(-)} - J_{sr(i,j)}^{k+1/2}}{\alpha^{(+)}}, \tag{19}$$

$$E_{\phi(i,j)}^{k+1} = \frac{\frac{1}{\Delta z}\left[H_{r(i+1,j)}^{k+1/2} - H_{r(i,j)}^{k+1/2}\right] - \frac{1}{\Delta r}\left[H_{z(i,j+1)}^{k+1/2} - H_{z(i,j)}^{k+1/2}\right] - E_{\phi(i,j)}^{k}\alpha^{(-)} - J_{s\phi(i,j)}^{k+1/2}}{\alpha^{(+)}}, \tag{20}$$

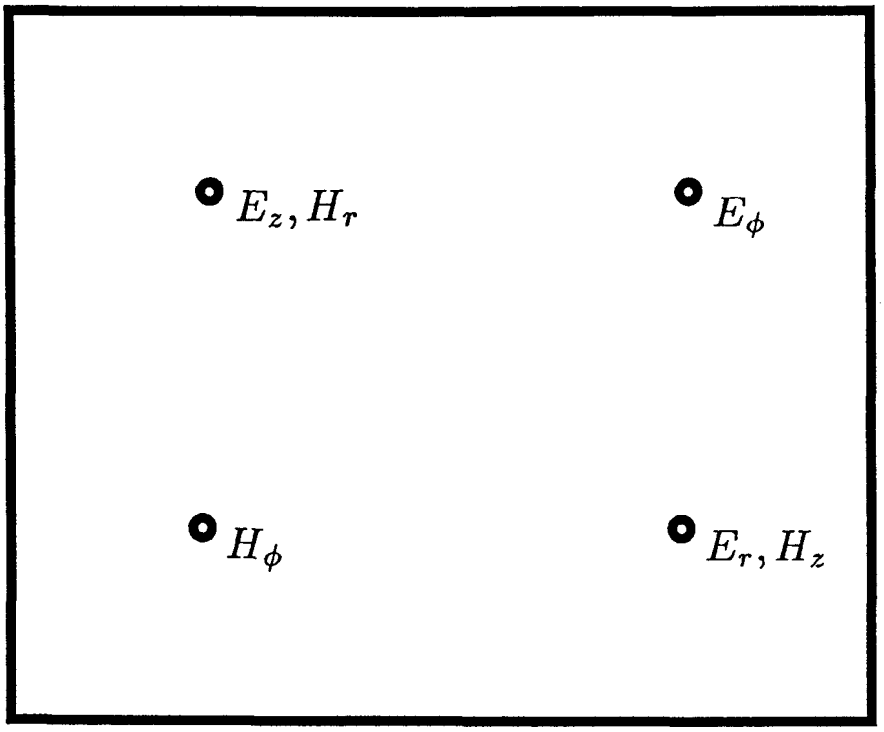

Fig. 3. Spatial distribution of field components in AMOS computational cell. Distribution allows all spatial derivatives in curl equations to be central-differenced.

$$E^{k+1}_{z(i,j)} = \frac{\frac{1}{j\Delta r}\left[(j+\frac{1}{2})H^{k+1/2}_{\phi(i,j+1)} - (j-\frac{1}{2})H^{k+1/2}_{\phi(i,j)}\right] \mp \frac{m}{j\Delta r}H^{k+1/2}_{r(i,j)} - E^{k}_{z(i,j)}\alpha^{(-)} - J^{k+1/2}_{sz(i,j)}}{\alpha^{(+)}}, \tag{21}$$

$$H^{k+1/2}_{r(i,j)} = \frac{\frac{\pm m}{j\Delta r}E^{k}_{z(i,j)} + \frac{1}{\Delta z}\left[E^{k}_{\phi(i,j)} - E^{k}_{\phi(i-1,j)}\right] + \frac{\mu(i,j)}{\Delta t}H^{k-1/2}_{r(i,j)} + K^{k}_{sr(i,j)}}{\frac{\mu(i,j)}{\Delta t}}, \tag{22}$$

$$H^{k+1/2}_{\phi(i,j)} = \frac{\frac{1}{\Delta r}\left[E^{k}_{z(i,j)} - E^{k}_{z(i,j-1)}\right] - \frac{1}{\Delta z}\left[E^{k}_{r(i,j)} - E^{k}_{r(i-1,j)}\right] + \frac{\mu(i,j)}{\Delta t}H^{k-1/2}_{\phi(i,j)} + K^{k}_{s\phi(i,j)}}{\frac{\mu(i,j)}{\Delta t}}, \tag{23}$$

$$H^{k+1/2}_{z(i,j)} = \frac{\frac{-1}{(j-\frac{1}{2})\Delta r}\left[jE^{k}_{\phi(i,j)} - (j-1)E^{k}_{\phi(i,j-1)}\right] \mp \frac{m}{(j-\frac{1}{2})\Delta r}E^{k}_{r(i,j)} + \frac{\mu(i,j)}{\Delta t}H^{k-1/2}_{z(i,j)} + K^{k}_{sz(i,j)}}{\frac{\mu(i,j)}{\Delta t}}, \tag{24}$$

where $\alpha^{(\pm)} = \frac{\sigma(i,j)}{2} \pm \frac{\epsilon(i,j)}{\Delta t}$. In Eqns. (19)-(24) we have replaced the superscripts p and q with superscripts $k-1/2$, k, $k+1/2$, and $k+1$ indicating the time step, and a parenthetical pair of subscripts has been added to indicate the spatial positions of the various field components on the finite difference grid. The first subscript indicates the component, as before in Eqns. (13)-(18), except in the case of the sources, where the first subscript is an s indicating that the field is a source field, and the second subscript indicates the component. Whether one is solving for the p or q part of a given component is determined by which equation set is being simulated, and this in turn is determined by which set of signs are used in Eqns. (19)-(24). The choice of coefficients used in (19)-(24) follows from the cell positioning shown in Fig. 4.

Initially, all fields are set to zero, or possibly some user defined initial field configuration, and the simulation clock is zeroed. Solution proceeds by first solving for the fields that exist at time step 1/2, $\vec{H}$ ($\vec{J}_s$ is supplied by the user), then solving for the fields at time step 1, $\vec{E}$ ($\vec{K}_s$ is supplied by the user), then time step 3/2, etc.

3. Calculation of Wake Potentials and Impedances

Consider the geometry illustrated in Fig. 5. The geometry that we are interested in is cylindrically symmetric, with the z-axis colinear with the axis of rotation. Let the source

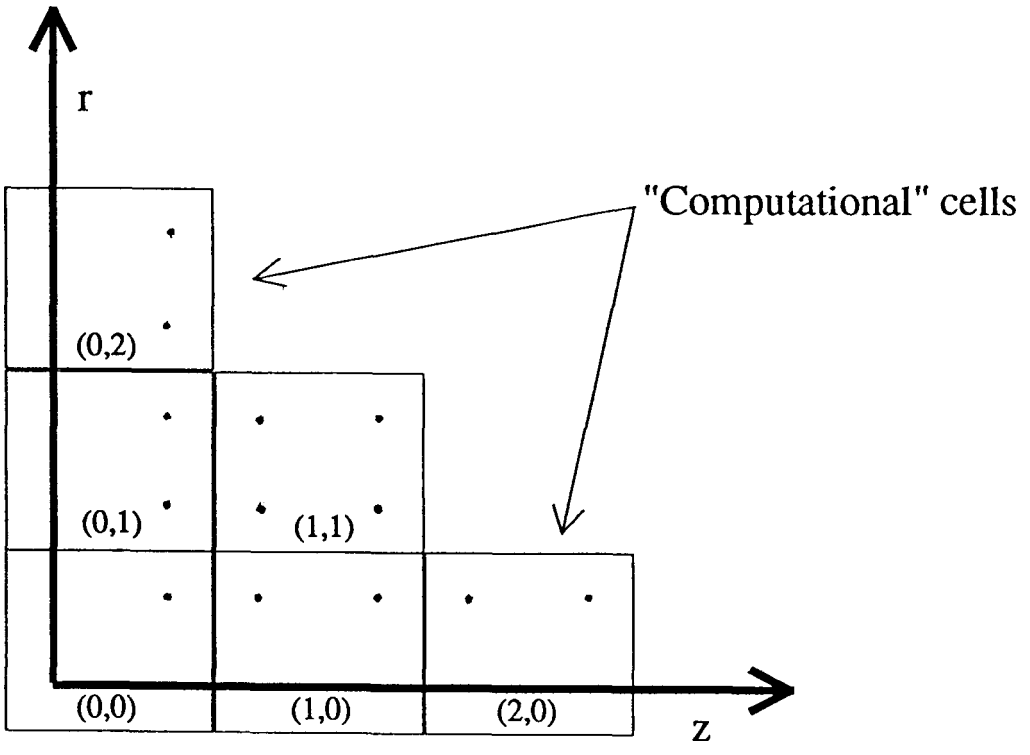

Fig. 4. Location and orientation of coordinate axes relative to the placement of the computational cells that make up the finite difference grid. The numbered pairs indicate the (i, j) indices for each cell.

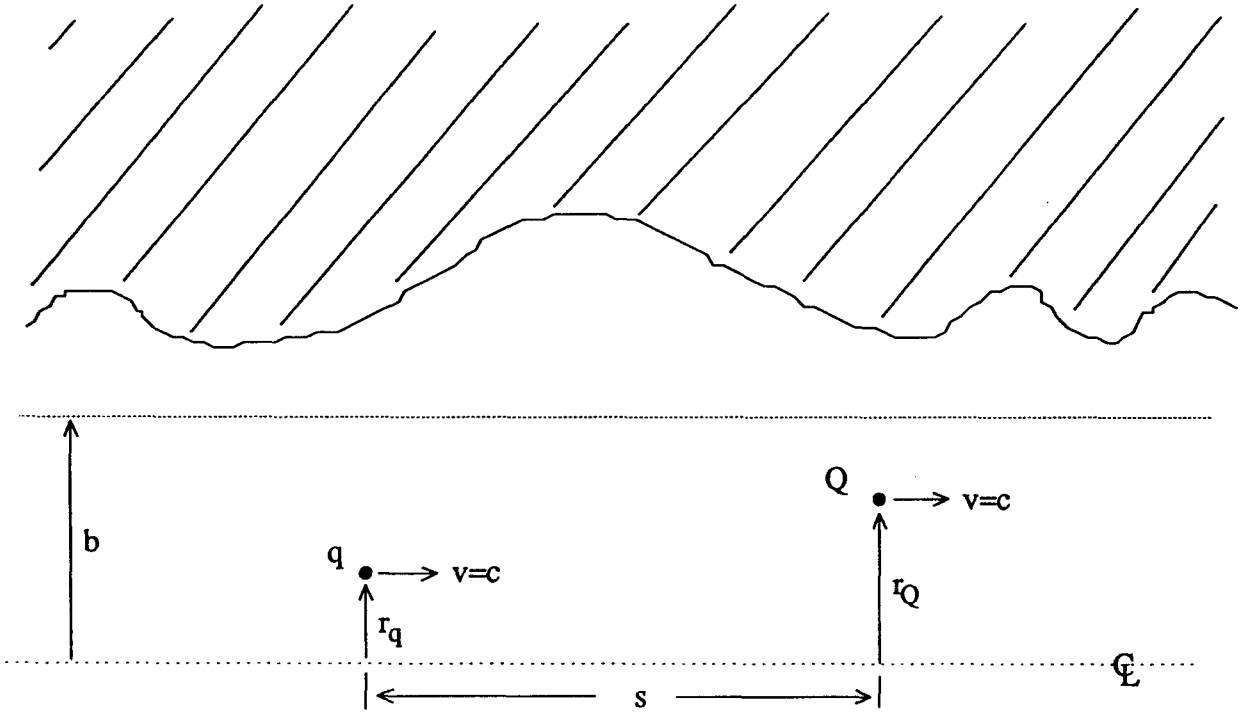

Fig. 5. Geometry assumed in the derivation of Eqn. (26) from Eqn. (25). The structure is assumed to be rotationally symmetric, and it is homogeneous (usually vacuum) in the region $r < b$. The distance s is positive for the test charge trailing the source charge.

of all fields in the problem be a charge Q, which will be referred to as the source charge. Assume that Q moves axially with a velocity of $v = c = 2.998 \times 10^8$ (m/s), and let Q have coordinates $(r, \phi, z) = (r_Q, 0, z_Q)$, where $z_Q = ct$. The impulse wake potential is then defined as

$$\vec{W}_\delta(s; r_Q, r, \phi) = \frac{1}{Q} \int_{-\infty}^{\infty} \left[\vec{E}(r, \phi, z, t; r_Q) + \eta_o \hat{k} \times \vec{H}(r, \phi, z, t; r_Q) \right] \Big|_{t=\frac{z+s}{c}} dz, \tag{25}$$

where $\eta_o = 377\Omega$ is the free space impedance, and $\hat{k}$ is a unit vector in the axial direction. Thus, $qQ\vec{W}_\delta$ is the integral of the Lorentz force that a charge q would experience traveling at a fixed position relative to the source charge, that position given by $(r, \phi, z_Q - s)$. It can be shown that Eqn. (25) may be written as a sum over azimuthal modes of the form

$$\vec{W}_\delta(s) = \sum_{m=0}^{\infty} \left(\frac{r}{b}\right)^m \left(\frac{r_Q}{b}\right)^m \left[\hat{k} \frac{dw_{cm}}{ds} \cos(m\phi) - \hat{\phi} \frac{m}{r} w_{cm} \sin(m\phi) + \hat{r} \frac{m}{r} w_{cm} \cos(m\phi) \right]. \tag{26}$$

w_{cm} is called the *characteristic* impulse wake potential of multipole m, and is defined by the expression

$$\frac{dw_{cm}(s)}{ds} = \frac{1}{Q} \int_{-\infty}^{\infty} E_z^p(b, z, t; b) \Big|_{t=\frac{z+s}{c}} dz, \tag{27}$$

where $E_z^p(b, z, t; b)$ is the axial multipole electric field that appears in Eqns. (13)-(18) evaluated at $r = b$, and with the source charge Q at $r_Q = b$. Thus, the individual multipole contributions to the total vector wake potential for any set of coordinates r_Q, r, and ϕ satisfying $r_Q, r \leq b$ may be computed by evaluating w_{cm} and its derivative using Eqn. (27), and then using Eqn. (26).

To compute the total potential at a particular point in a charge bunch, we introduce the concept of a bunch wake potential, which is simply a convolution of the impulse wake potential with the charge distribution, i.e.,

$$\vec{W}_B(s; r, \phi) = \int_{s'=-\infty}^{\infty} \int_{r'=0}^{b} \int_{\phi'=0}^{2\pi} \vec{W}_\delta(s - s'; r', r, \phi - \phi') \rho(s', r', \phi') r' dr' d\phi' ds', \tag{28}$$

where ρ is the spatial charge density in the bunch, as measured in the beam frame. The definition of the parameter s is identical to that used in the original definition of the impulse wake potential, if one measures s from some fixed point in the bunch. Thus, the impulse wake potential is used as a Green's function to compute the bunch wake potential. Taking the Fourier transform of $\vec{W}_B$ over the variable s, and applying the convolution theorem, yields

$$\vec{W}_B(k) = \int_{r'=0}^{b} \int_{\phi'}^{2\pi} \vec{W}_\delta(k; r', r, \phi - \phi')\rho(k, r', \phi')r'dr'd\phi', \tag{29}$$

where the Fourier transform is denoted by the use of the frequency domain variable k in place of s. Multiplying ρ by c, and dividing $\vec{W}_\delta$ by c, Eqn. (29) may be written in the form

$$\vec{W}_B(k) = \int_{r'=0}^{b} \int_{\phi'=0}^{2\pi} \vec{Z}(k; r', r, \phi - \phi')J_z(k, r', \phi')r'dr'd\phi', \tag{30}$$

where J_z is the z-directed current density, with units of A/m because we have taken a transform over the s variable, and $\vec{Z}$ is the vector impedance, with units of ohms. As defined by Eqn. (30) the impedance is given by the relation

$$\vec{Z}(\omega) = \frac{1}{c}\vec{W}_\delta(\omega/c). \tag{31}$$

In the preceeding discussion, we have laid out the definitions of the wake potential and impedance. In practice, the computation of these quantities is subject to a number of difficulties which restrict the class of geometries for which they can be calculated accurately. Although these difficulties will not be elaborated upon in this article, they will be discussed in a later paper. In addition, although Eqns. (26) and (31) follow from the simple definition in Eqn. (25), slightly different definitions of the impulse wake potential and impedance may be found in the literature. In a concession to established convention, the impedance that is computed by AMOS differs from Eqn. (31) in that the transverse components are multiplied by $-i$. AMOS computes the spectral limits indicated by the mesh size and

the source bunch width, and applies the most restrictive to limit the highest frequency at which values of $\vec{Z}$ are output.

4. AMOS Applications

AMOS has been applied to a variety of problems involving accelerator cavities. The typical questions that AMOS is used to answer concern the frequencies of cavity resonances and the design variations that would reduce beam–resonance coupling. We will discuss work on induction cells from three different accelerators: (1) ATA, (2) SNOMAD, and (3) DARHT.

The ATA induction cell [6] (Fig. 6) was one of the first cells studied using AMOS. The primary thrust in this investigation was to determine which of the cavity dipole ($m = 1$) resonances could be expected to couple strongly enough to the beam to cause beam oscillations. These beam breakup (BBU) modes can lead to beam loss on the walls of the accelerator beampipe. It was possible to determine which cavity modes would be excited by an electron beam transiting the accelerating gap by driving a short pulse of current across the gap at the beampipe radius (see Fig. 6) and then taking the Fourier transform of the resulting axial electric fields in the gap. Also, by computing the wake potential and the cavity impedance, we were able to determine the strength of this beam–cavity coupling. This procedure yielded the discovery of two dipole modes, both quite near in frequency to the TE_{11} cutoff frequency, which were not appreciably damped by the ferrite in the cavity. In the absence of a high frequency ferrite model, the ferrite was approximated by an impedance boundary condition.

The first mode may be expected in any perpendicular joint between a pipe and a radial line, and it is located in the vicinity of the accelerating gap entrance into the beampipe. A field plot for this mode is shown in Fig. 7a. Since this mode is localized near the joint, and is evanescent into both the beampipe and the radial line, it follows that the placement of ferrite pucks in the ATA cell shown in Fig. 6 will not damp this mode. Fortunately,

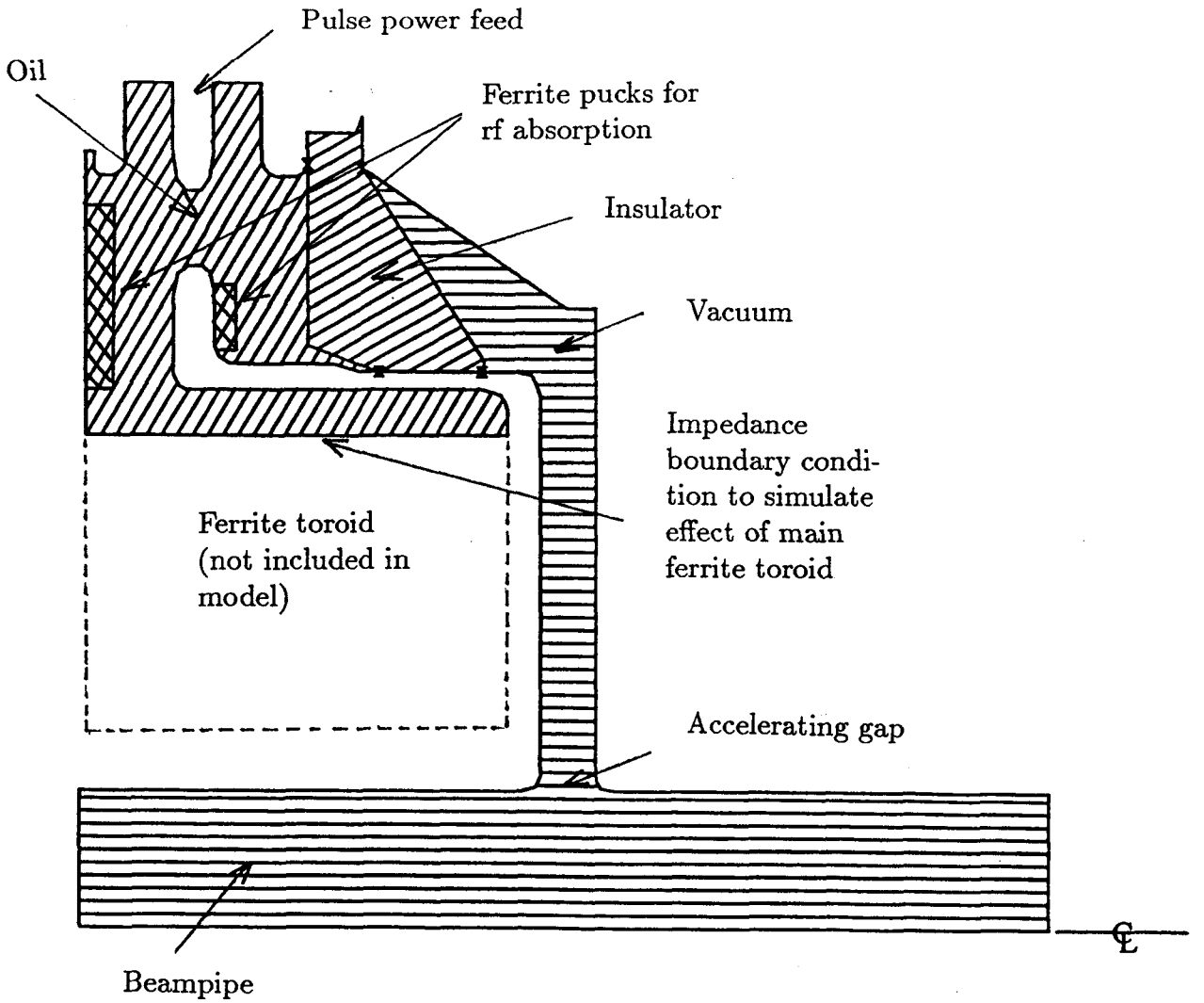

Fig. 6. DRAGON rendering of azimuthal cross section of ATA cell (actual cell is rotationally symmetric about the axis, except for the pulse power feed line). The electron beam travels through the beampipe on axis, and experiences an accelerating voltage as it traverses the gap. This voltage is induced on the gap by a pulse delivered by the pulse power input cables. The large ferrite toroid acts as an inductive load to the pulse power drive; it is required to match the cell impedance with the impedance of the pulse power feed line. The ferrite pucks are placed in the cell at strategic points to damp out undesirable rf resonances in the cavity.

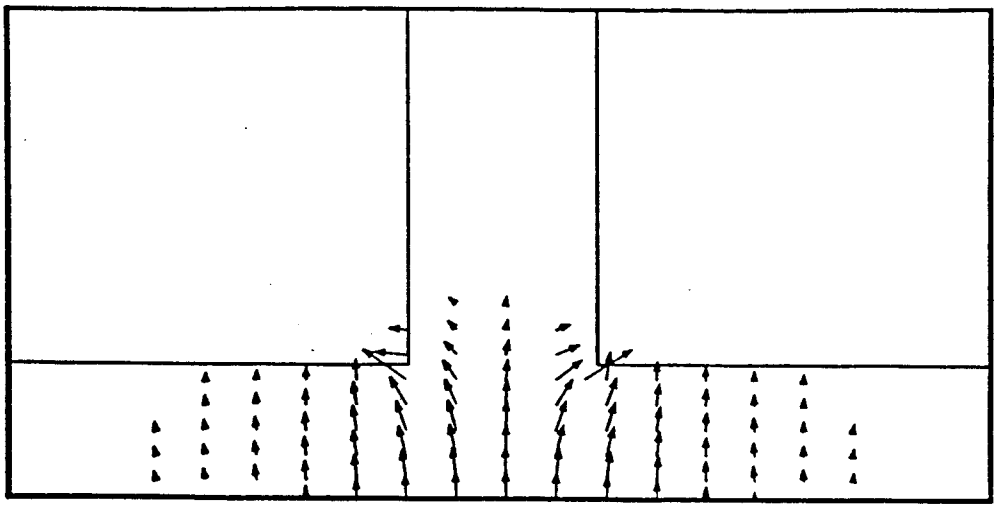

(a)

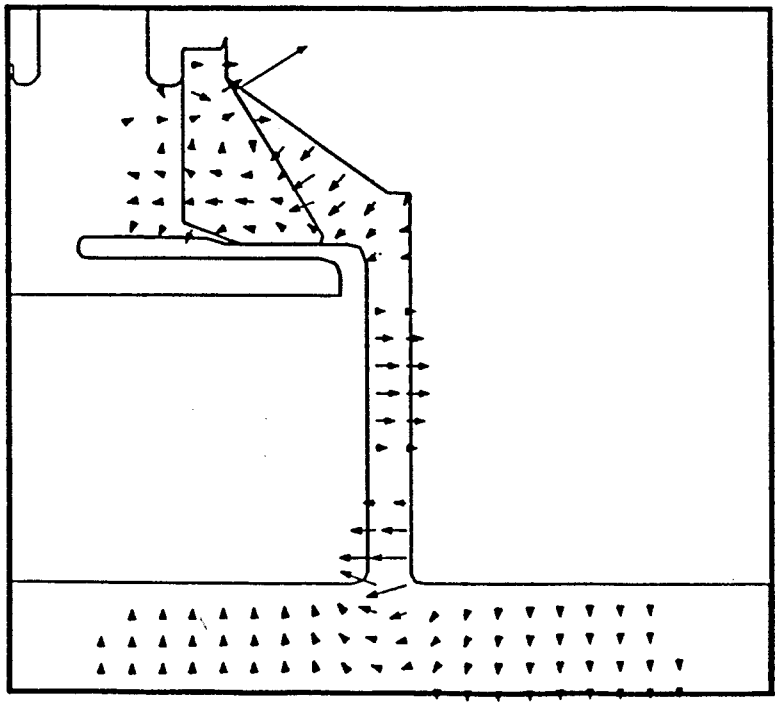

(b)

Fig. 7. Plots of two high-Q dipole modes produced by AMOS in simulations of an ATA induction cell: (a) mode localized near the joint between the beamline and the accelerating gap, and (b) a mode evanescent in the oil behind the insulator. The plots show the direction and magnitude (length of vector tail) of the electric field in an azimuthal cross section of the cell. The symmetry axis is at the bottom of each plot. Note that mode (a) does not couple strongly to a transiting electron beam, if the gap is narrow, because the sign reversal of the axial electric field in the gap causes whatever energy that is put into the mode while the beam is moving toward the gap to be removed again as the beam passes and moves away from the gap. By the same argument mode (b) should be strongly excited by the beam.

because of the asymmetry in the axial field about the center of the gap, this mode does not couple significantly to a transiting charged particle beam unless the gap is wide enough that the transit time is significant as compared to the mode oscillation period.

The second mode of interest is possibly unique to the ATA cell geometry, and a field plot of this mode is shown in Fig. 7b. This mode is also not damped by the ferrite in the cell, as it is evanescent beyond the insulator. In principle this mode should couple strongly to the beam because the axial field is of one sign (symmetric) in the gap; however, the experimental evidence for this mode is inconclusive. It may be that the proximity of the mode to the beampipe cutoff is allowing some of the mode energy to be carried out of the cavity in the form of traveling waves in the pipe so that the mode amplitude cannot reach an appreciable level. AMOS has been used to suggest modifications to the ATA cell geometry and changes in the ferrite position which will reduce the effects of all modes which may interact with the beam.

Another application that has yielded interesting results is the SNOMAD accelerator cell [7] (Fig. 8). This cell is significantly smaller than the ATA cell. Since there was an isolated cell available for testing, we have been able to compare AMOS predictions of mode locations directly with experimental measurements. Modes up to m=4 (modes that have a ϕ-dependence of the form $\cos(4\phi)$ or $\sin(4\phi)$) have been computed and compared with measurements, and these results are shown in Table 1. Agreement with experiment for this case is excellent. When the ferrite is unmasked, agreement with measurement is more qualitative. This is due to the use of an impedance boundary condition to simulate the effects of the ferrite. Results of this type are important benchmarks for AMOS; they have provided some of the earliest tests of the code against experimental measurements on a complex geometry.

The last application that we will discuss is the DARHT induction cell [8]. The DARHT accelerator is being built at LANL. It produces an electron beam that will be focussed on a tantalum target to produce x-rays for photography of extremely dense materials. AMOS

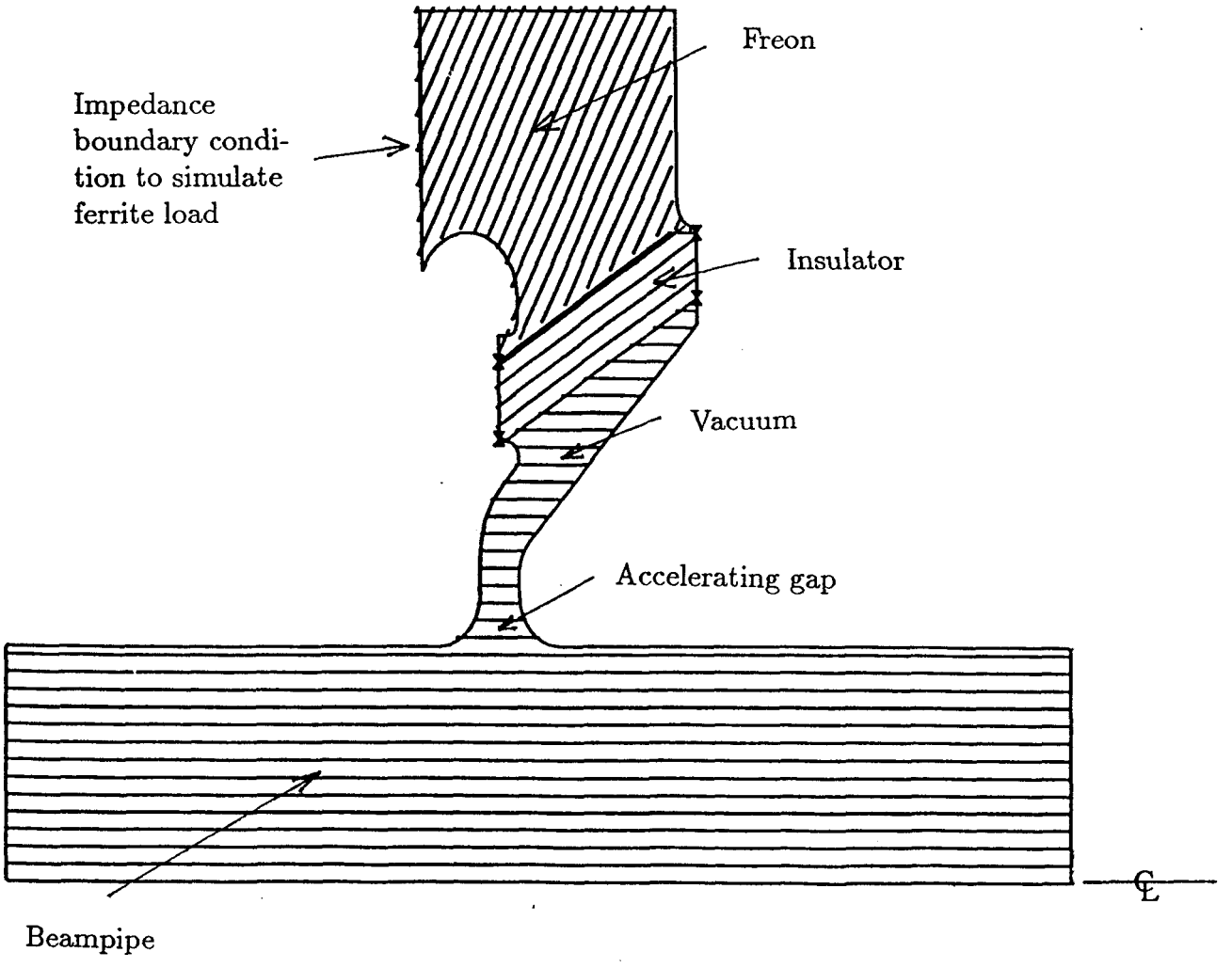

Fig. 8. DRAGON rendering of azimuthal cross section of SNOMAD induction cell. Experimental measurements of the resonant mode frequencies were made for this cell, and these values were compared to AMOS simulations. For the data shown in Table 1 the ferrite was masked by a perfect conductor, and the oil and insulator were removed.

Mode	Calculated Resonant Frequency	Measured Resonant Frequency
TM010	.66 (GHz)	.674 (GHz)
TM020	2.52	2.539
TM030	3.72	3.736
TM110	1.35	1.341
TM120	2.66	2.696 2.721
TM210	2.20	2.185
TM220	3.10	3.130
TM310	2.82	2.833
TM320	3.73	3.756
TM410	3.35	3.36

Table 1. Comparison of experimental measurements and AMOS simulation results for the location of resonant modes in the SNOMAD induction cell. For these comparisons, the ferrite was masked with a perfect conductor, and the insulator and oil were removed.

was used to assist in the design of the prototype DARHT induction cavity. The preliminary DARHT induction cell design is shown in Fig. 9a. Several of the resonant modes exhibited unacceptably high coupling impedances with the electron beam, and AMOS was used to study the effects that geometric and material modifications would have on these resonances. The optimal design as determined using AMOS is shown in Fig. 9b. The final design differs slightly from the AMOS design because of pulse power and other considerations. For instance, sharp corners were rounded off to optimize the cell performance at high drive voltages. The corresponding longitudinal and transverse impedances for the preliminary and AMOS designs are compared in Fig. 10. The impedance of a cell is related to the strength of the interaction between the electron beam and the cell. The longitudinal impedance measures the coupling of the axial motion of the beam to cavity modes; the transverse impedance measures the coupling of beam motion transverse to the beampipe axis with cavity modes. In general, one would like the coupling impedances in both directions to be as small as possible to minimize the effects of cavity resonances on the beam. During the process of optimizing the cavity design using AMOS, it was discovered that the coupling impedances, especially for the high frequency modes, were affected strongly by both the positioning and the dielectric constant of the insulator, as well as the shape of the angular reflector at the top of the cell. Several parameters were varied over a range constrained by the fabrication requirements until the corresponding impedances were minimized.

In addition to the applications detailed above, AMOS has also been used to study various aspects of other accelerators. These include SLIA (Spiral Line Induction Accelerator), ETA-II, the relativistic klystron and HGA (High Gradient Accelerator), the dielectric wakefield accelerator concept, and study of a proposed linac for heavy ion fusion. work.

5. Ongoing Development

In modeling objects with complex geometries, it may be important to represent the

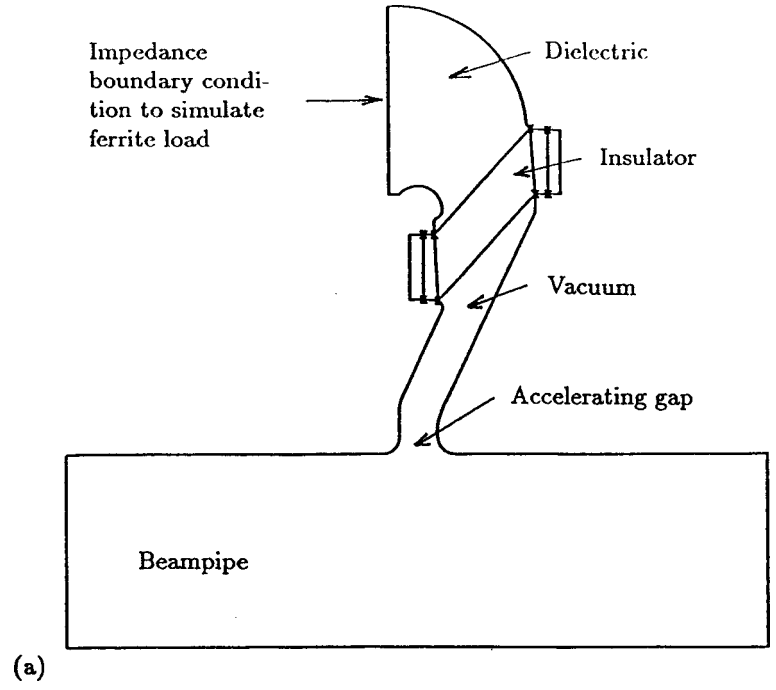

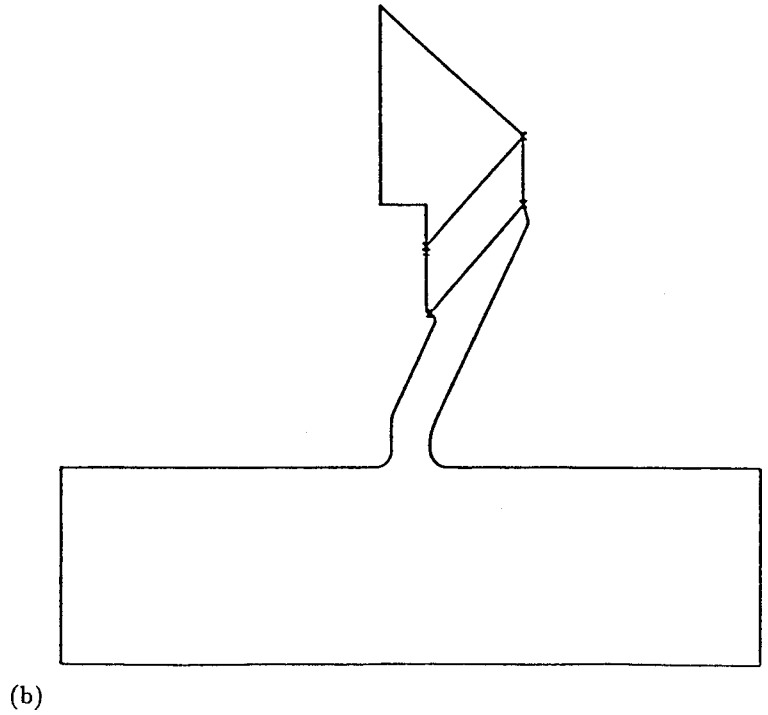

Fig. 9. Diagram of (a) preliminary design of DARHT induction cell, and (b) design after optimization using AMOS. Design parameters such as shape of the reflector and the shape and material properties of the insulator were varied to optimize the rf characteristics of the cell for accelerator applications.

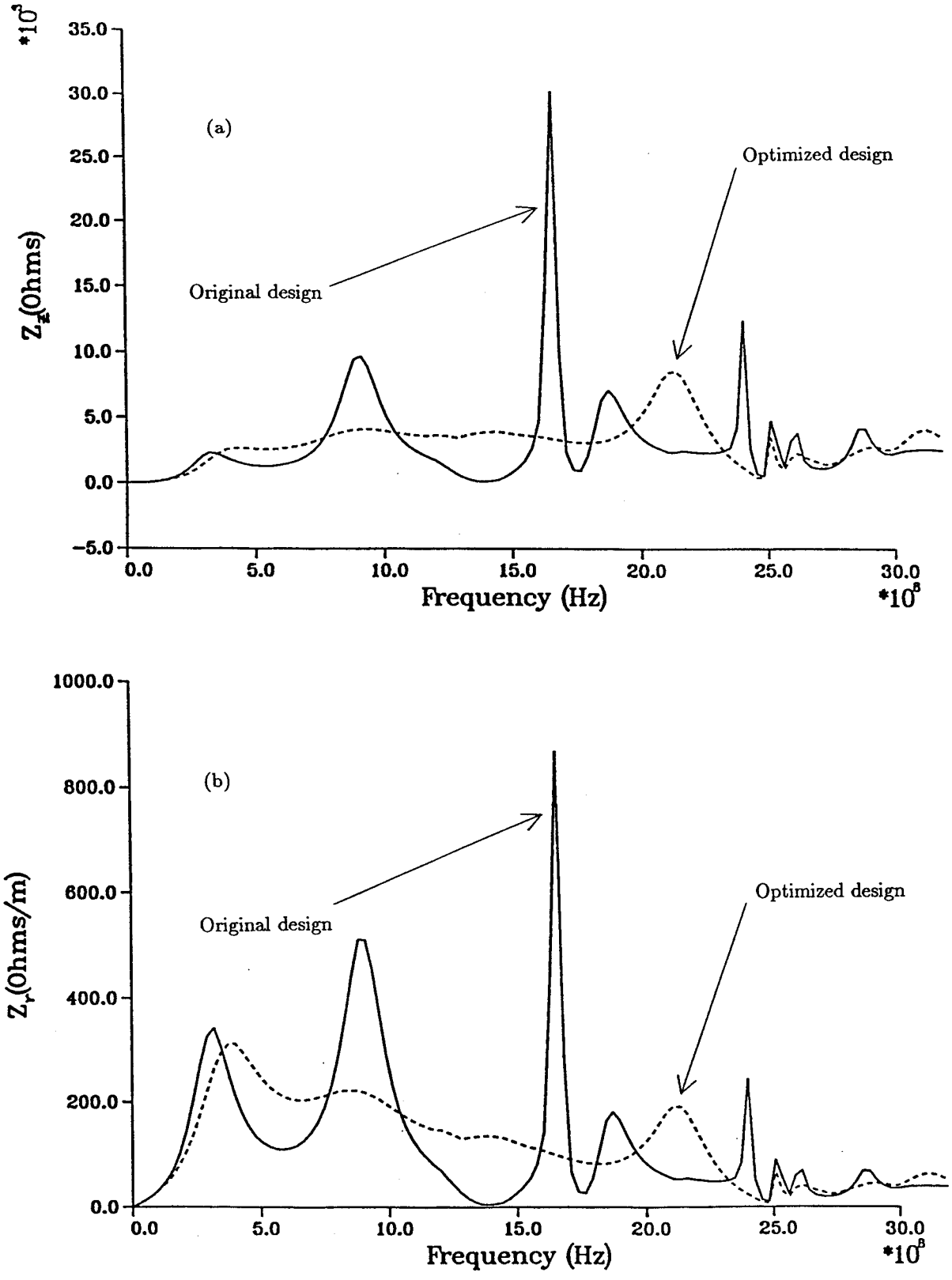

Fig. 10. (a) Longitudinal, monopole ($m = 0$) and (b) transverse, dipole ($m = 1$) coupling impedances are compared for the original and optimized DARHT induction cells. The impedance is a measure of the coupling between modes in the cell and the electron beam. It is desirable to have all components of the impedance as low as possible over a broad frequency range.

boundaries of simulation space more accurately with the elements of an irregular grid. We are currently upgrading AMOS so that one may, if necessary, capture the essence of these details.

The thrust of the development work is in directly implementing an update scheme to an irregular grid using the integral form of Maxwell's time dependent curl equations. This involves the placement of field components on a body fitting non-orthogonal grid and on a dual grid, orthogonal to the first grid. This appears to be an efficient method since one may localize the irregular portion of the grid to the boundaries, allowing one to vectorize significant subregions of the body and to update on finite difference cells. This procedure, in effect, retains all of the computational advantages of the present code. Further, since absorbing boundary conditions (Mur [9]) work well for $d\theta$ near normal incidence to a cell face, the elements of the irregular grid are a more natural choice than finite difference cells for modeling radiation conditions on an oblique surface boundary.

The authors are also involved in the development of ferrite models that are suitable for time-domain simulation. Most of the current effort is focussed on a linear, high frequency, tensor permeability model. An experimental program has been undertaken to measure the frequency dependent coefficients of the tensor for various soft ferrites under a variety of bias conditions. These expermental data are being used to determine parameters in a theoretical model, and this model is being implemented as a module in AMOS. A low frequency, nonlinear, ferrite switching model has also been installed in AMOS. This model will be used to study the pulse power response of accelerator induction cavities, and it is currently undergoing extensive testing against experimental data taken on small cores of ATA and ETA-II ferrite. Both of these models will be in module form and will be removable from the code. This will ensure that problems which do not involve ferrite will not be slowed down by the additional calculations that are required by the ferrite models.

Various support software is being developed for AMOS, including output graphics and a more complete front end, or preprocessor. The completed user interface to AMOS will

simplify the generation of the entire input file (not just the geometry section as is currently the case), and will also automate the concatenation of the necessary AMOS modules to construct an executable version of AMOS which is suitable for any given problem.

6. Conclusions

AMOS is a FDTD electromagnetic simulation computer code for use in designing and studying accelerator cavities and other rotationally symmetric structures in beamlines. The code has a preprocessor for generating simulation grids from model geometries, and a computational postprocessor that computes wake potentials and cavity impedances from the AMOS field time histories. A graphical postprocessor that will plot time histories and vector field data is under development. AMOS has been applied to a variety of test problems involving simple canonical structures as well as to design problems with very complex geometries. As of the date of this conference the code had not yet been released into the public domain. However, we are interested in seeing the code used in a variety of accelerator applications, and interested persons are invited to contact the authors.

7. Acknowledgements

The authors would like to acknowledge Bernard Kulke (LLNL) for his contribution in performing the experiments on the SNOMAD cell, and Mike Burns (LANL) for carrying out the DARHT cell design calculations. We also acknowledge Clifford Shang (LLNL), who is carrying out the AMOS irregular-mesh upgrade, and Ron Schmucker (LLNL), who provided graphics software for the vector field plots.

References

[1] J. F. DeFord, G. D. Craig, and R. R. McLeod, "The AMOS (Azimuthal MOde Simulator) code," presented at the 1989 Particle Accelerator Conference, Chicago, IL, March 20-23, 1989. Also in proceedings of same meeting, to be published.

[2] P. B. Wilson, "Introduction of wakefields and wake potentials," *SLAC-PUB-4347, SLAC/AP-66*, Jan., 1989.

[3] K. L. F. Bane, P. B. Wilson, and T. Weiland, "Wake fields and wake field acceleration," *Physics of High Energy Particle Accelerators*, BNL/SUNY Summer School, pp. 875-928, 1983

[4] K. L. F. Bane, "Wakefield effects in a linear collider," *SLAC-PUB-4169*, Dec. 1986.
[5] K. Yee, "Numerical solution of initial boundary value problems involving Maxwell's equations in isotropic media," *IEEE Transactions on Antennas and Propagation*, **AP-14**, May, 1966, pp. 302-307.
[6] R. J. Briggs, et al., "Theoretical and experimental investigation of the interaction impedances and Q values of the accelerating cells in the Advanced Test Accelerator," *Particle Accelerators*, **18**, 1985, pp. 41-62.
[7] B. Kulke, G. Craig, and D. Aalberts, "Prediction and measurement of potential BBU resonances in an accelerator cell," presented at the Spring Meeting of the APS, Washington D.C., Apr. 16-19, 1990.
[8] M. Burns, et al., "Design of the prototype accelerator cell for the DARHT induction linacs," presented at the APS Division of Plasma Physics, Anaheim, CA, Nov. 13-17, 1989.
[9] G. Mur, "Absorbing boundary conditions for the finite difference approximation of the time-domain electromagnetic field equations," *IEEE Transactions on Electromagnetic Compatibility*, **EMC-23**, Nov., 1981, pp. 377-382.